



This discussion paper is/has been under review for the journal Atmospheric Measurement Techniques (AMT). Please refer to the corresponding final paper in AMT if available.

A Fabry–Perot interferometer based camera for two-dimensional mapping of SO₂ distributions

J. Kuhn¹, N. Bobrowski¹, P. Lübcke¹, L. Vogel², and U. Platt¹

¹Institute of Environmental Physics, University of Heidelberg, Heidelberg, Germany

²Earth Observation Science, Space Research Centre, University of Leicester, Leicester, UK

Received: 19 January 2014 – Accepted: 13 May 2014 – Published: 22 May 2014

Correspondence to: J. Kuhn (jkuhn@iup.uni-heidelberg.de)

Published by Copernicus Publications on behalf of the European Geosciences Union.

Title Page

Abstract

Introduction

Conclusions

References

Tables

Figures



Back

Close

Full Screen / Esc

Printer-friendly Version

Interactive Discussion



Abstract

We examine a new imaging method for the remote sensing of volcanic gases, which relies on the regularly spaced narrow-band absorption structures in the UV-VIS of many molecules. A Fabry–Perot interferometer (FPI) is used to compare the scattered sunlight radiance at wavelengths corresponding to absorption bands with the radiance at wavelengths in between the bands, thereby identifying and quantifying the gas. In this first theoretical study, we present sample calculations for the detection of sulfur dioxide (SO₂). Optimum values for the FPI set-up parameters are proposed. Further, the performance of the FPI method is compared to SO₂ cameras. We show that camera systems using a FPI are far less influenced by changes in atmospheric radiative transfer (e.g. due to aerosol) and have a great potential as a future technique to examine emissions of SO₂ (or other gases) from volcanic sources and other point sources.

1 Introduction

SO₂ emission rates are routinely measured as a monitoring parameter at many volcanoes (Galle et al., 2010). The chemical lifetime of SO₂, which can account for up to 25 % of the total emitted volcanic gas volume (Textor et al., 2004), is on the order of days and background concentrations in the ambient atmosphere are usually very low. Therefore volcanic SO₂ can easily be measured by remote sensing techniques and it often serves as a dilution tracer when studying the chemistry of more reactive gases emitted by volcanoes (e.g. Oppenheimer et al., 1998; von Glasow et al., 2009).

Besides COrrrelation SPECTroscopy (COSPEC, Moffat and Millan, 1971), Differential Optical Absorption Spectroscopy (DOAS, Platt and Stutz, 2008) has become a more and more common technique to examine volcanic SO₂ emissions. The DOAS technique allows the application of compact, portable devices and is further able to measure other gas species (e.g. BrO, OCIO, O₃) simultaneously. However, typical DOAS (and COSPEC) measurements provide data only in a single viewing direction.

AMTD

7, 5117–5145, 2014

FPI for SO₂ detection

J. Kuhn et al.

Title Page

Abstract

Introduction

Conclusions

References

Tables

Figures

◀

▶

◀

▶

Back

Close

Full Screen / Esc

Printer-friendly Version

Interactive Discussion



FPI for SO₂ detection

J. Kuhn et al.

Title Page

Abstract

Introduction

Conclusions

References

Tables

Figures



Back

Close

Full Screen / Esc

Printer-friendly Version

Interactive Discussion



As mentioned already in Kern et al. (2010b), regularly spaced narrow-band absorption structures of SO₂ allow measuring SO₂ by using a Fabry–Perot interferometer (FPI). Radiances at wavelengths of maximum narrow-band SO₂ absorption can be compared to radiances at wavelengths in between these maxima. Thereby, the above mentioned errors of the SO₂ camera technique due to radiative transfer effects could be drastically reduced (Sect. 3). The FPI technique introduced here allows constructing simple and low-cost devices, which can record one- or two-dimensional data with high temporal resolution (Sect. 4).

The correlation between the spectral FPI transmission and periodic spectra was first used to study molecular spectra (e.g. Barrett and Myers, 1971). Later, several approaches to identify and quantify gases by FPI correlation were reported (mainly in the IR, see e.g. Wilson et al., 2007; Vargas-Rodriguez and Rutt, 2009). In contrast to previous studies, this study focuses on UV detection and imaging of volcanic gas emissions.

2 SO₂ camera and FPI measurement principle

The conventional SO₂ camera uses two interference filters (A and B, see Fig. 1) to compare the scattered sunlight radiances of two neighbouring UV wavelength ranges for a certain field of view (FOV, typically around 20°). In the wavelength range of filter A (~ 310–320 nm, filter transmission curves according to Lübcke et al., 2013) SO₂ is the dominant gaseous absorber in the plume. For each pixel the radiance measured with filter A in front of the detector is determined by the quantum yield $Q(\lambda)$ of the detector (which is set to unity for this theoretical study), the transmission curve $T_A(\lambda)$ of filter A, and the incident spectral radiance $I_S(\lambda)$:

$$I_A = \int I_S(\lambda) \cdot T_A(\lambda) \cdot Q(\lambda) d\lambda \quad (1)$$

I_A is compared to a reference radiance $I_{A,0}$, also measured through filter A:

$$I_{A,0} = \int I_{S,0}(\lambda) \cdot T_A(\lambda) \cdot Q(\lambda) d\lambda \quad (2)$$

$I_{S,0}(\lambda)$ is supposed to be the spectral radiance with the radiation not passing through the absorber (the volcanic plume). Since it is generally not possible to measure $I_{A,0}$ with the same viewing direction as I_A , a measurement in a slightly different direction outside the plume is commonly used as approximation.

Via the Beer–Lambert’s law these two radiance values are linked to the optical density τ_A of the volcanic plume for each pixel in the wavelength range of Filter A:

$$\tau_A = -\log \frac{I_A}{I_{A,0}} = \tau_{SO_2,A} + \tau_{other,A} \quad (3)$$

with

$$\tau_{SO_2,A} = \bar{\sigma}_{SO_2,A} \cdot S_{SO_2} \quad (4)$$

The plume optical density τ_A in the wavelength window of filter A is a function of the SO_2 absorption $\tau_{SO_2,A}$ and the contribution of other extinctive effects $\tau_{other,A}$ (e.g. scattering at plume aerosol). $\bar{\sigma}_{SO_2,A}$ is the weighted absorption cross section of SO_2 averaged over the wavelength range of filter A. S_{SO_2} is the SO_2 column density.

In an analogous way τ_B is the optical density measured through filter B (~ 325–340 nm) where the SO_2 absorption is significantly smaller (see Fig. 1):

$$\tau_B = -\log \frac{I_B}{I_{B,0}} = \tau_{SO_2,B} + \tau_{other,B} \quad (5)$$

τ_B is subtracted from τ_A in order to obtain a signal which only depends on SO_2 absorption. This correction assumed that all extinction originating from other effects than SO_2

absorption are broad-band (independent of wavelength in the regarded spectral range, i.e. $\tau_{\text{other,A}} \approx \tau_{\text{other,B}}$):

$$\tilde{\tau} = \text{AA} = \tau_A - \tau_B \approx \tau_{\text{SO}_2,\text{A}} - \tau_{\text{SO}_2,\text{B}} = \left(\bar{\sigma}_{\text{SO}_2,\text{A}} - \bar{\sigma}_{\text{SO}_2,\text{B}} \right) \cdot S_{\text{SO}_2} \quad (6)$$

$\tilde{\tau}$ is called Apparent Absorbance (AA) and ideally proportional to S_{SO_2} . The weighted SO_2 absorption cross sections ($\bar{\sigma}_{\text{SO}_2,\text{A}}$, $\bar{\sigma}_{\text{SO}_2,\text{B}}$) can be determined using calibration cells (e.g. Mori and Burton, 2006). Another possible calibration method for the SO_2 camera is using additional DOAS measurements (e.g. Lübcke et al., 2013).

By using a FPI in our new, proposed instrument more detailed spectral information is taken into account. Thus a higher SO_2 sensitivity is reached. Moreover, interferences of the SO_2 measurement with radiative transfer effects such as wavelength dependent (aerosol) scattering and changing ozone background are drastically reduced.

A FPI consists of two plane parallel surfaces with reflectance R at distance d (see Fig. 2). Incident radiation is split up in a reflected and a transmitted part at the individual surfaces. The partial beams pass through different optical path lengths between the two surfaces before leaving the FPI. For radiation of wavelength λ and a refractive index n of the medium between the surfaces, this results in a phase difference

$$\delta(\lambda; n, d, \alpha) = 2\pi \cdot \frac{2nd}{\lambda} \cdot \cos \alpha \quad (7)$$

between two consecutively transmitted (or reflected) partial beams. α is the angle between the propagation direction of the partial beams and the surface normal in between the two surfaces. The reflectance R of the surfaces determines the finesse (F) (see Eq. 10) of the FPI. F is a measure for the number of partial beams, which effectively interfere with each other after being transmitted (or reflected) by the FPI ($F(R)$ increases monotonically). Superposition of all transmitted partial beams with their respective phase shifts and neglecting of absorption effects yields the transmission profile of the

FPI for SO_2 detection

J. Kuhn et al.

Title Page

Abstract

Introduction

Conclusions

References

Tables

Figures



Back

Close

Full Screen / Esc

Printer-friendly Version

Interactive Discussion



FPI (Perot and Fabry, 1899):

$$T_{\text{FPI}}(\lambda; d, n, \alpha, R) = \left[1 + C_F \cdot \sin^2 \left(\frac{\delta(\lambda)}{2} \right) \right]^{-1} \quad (8)$$

$$= \left[1 + C_F \cdot \sin^2 \left(\frac{2nd\pi}{\lambda} \cos \alpha \right) \right]^{-1} \quad (9)$$

5 with

$$C_F = \frac{4R}{(1-R)^2} \approx \frac{4 \cdot F^2}{\pi^2} \quad \text{or} \quad F \approx \frac{\pi\sqrt{R}}{1-R} \quad (10)$$

10 The approximation for F in Eq. (10) is only valid for $R > 0.5$. T_{FPI} is a periodic function of δ with maxima for δ attaining integer multiples of 2π . For an increasing finesse coefficient C_F and thus for increasing F or R , the spectral transmission maxima get sharper.

15 The periodic, comb shaped transmission structure of the FPI can be used to compare the radiance transmitted at wavelengths corresponding to the narrow band SO_2 absorption maxima with those corresponding to absorption minima by using appropriate FPI instrument parameters. In the simplest case two FPI settings are used. In one FPI setting (setting A, Fig. 1, lower panels) the parameters are chosen such that the transmission maxima of the FPI coincide with the maxima of the absorption structure of SO_2 . In another setting (setting B) the transmission maxima of the FPI coincide with the minima of the SO_2 absorption structure. Setting B is reached by changing δ . By
20 comparing the transmitted radiances recorded with FPI setting A and B the SO_2 column density can in principle be derived in a similar manner as with the SO_2 camera.

25 However, scattered solar radiation at wavelength ranges without narrow-band SO_2 absorption structure matching the FPI transmission has to be excluded. Towards shorter wavelengths with strong narrow-band absorption structure, the scattered solar radiance at ground level decreases very fast (mostly because of increasing absorption

FPI for SO_2 detection

J. Kuhn et al.

Title Page

Abstract

Introduction

Conclusions

References

Tables

Figures



Back

Close

Full Screen / Esc

Printer-friendly Version

Interactive Discussion



due to stratospheric ozone). For FPI SO₂ measurements in the regarded spectral range it is therefore sufficient to limit the measurement wavelength range towards longer wavelengths, where SO₂ absorption structures are too weak. This can be accomplished by a superimposed short-pass or band-pass interference filter (bpf) with transmission T_{bpf} (see Fig. 1, lower panels), which will be characterized by the largest transmitted wavelength λ_{cut} .

The radiance measured by the detector after having traversed the band-pass filter and the FPI in the setting $i = A, B$ is given by (compare Eq. 1):

$$I_{\text{FPI},i} = \int I_{\text{S}}(\lambda) \cdot T_{\text{FPI},i}(\lambda) \cdot T_{\text{bpf}}(\lambda) \cdot Q(\lambda) \, d\lambda \quad (11)$$

By comparing to reference measurements

$$I_{0,\text{FPI},i} = \int I_{\text{S},0}(\lambda) \cdot T_{\text{FPI},i}(\lambda) \cdot T_{\text{bpf}}(\lambda) \cdot Q(\lambda) \, d\lambda \quad (12)$$

the optical densities for the corresponding FPI transmissions are determined:

$$\tau_{\text{FPI},i} = -\log \frac{I_{\text{FPI},i}}{I_{0,\text{FPI},i}} = \tau_{\text{SO}_2,\text{FPI},i} + \tau_{\text{other},\text{FPI},i} \quad (13)$$

$\tau_{\text{SO}_2,\text{FPI},i}$ is the part of the SO₂ absorption τ_{SO_2} seen through the transmission profile of the respective FPI setting and therefore proportional to S_{SO_2} . When choosing setting A and B as described above $\tau_{\text{SO}_2,\text{FPI},A}$ and $\tau_{\text{SO}_2,\text{FPI},B}$ differ in the presence of SO₂, while $\tau_{\text{other},\text{FPI},i}$ is considered to be approximately the same for the two FPI settings. Similar as for the SO₂ camera we get:

$$\tilde{\tau}_{\text{FPI}} = \Delta A_{\text{FPI}} = \tau_{\text{FPI},A} - \tau_{\text{FPI},B} \propto \tau_{\text{SO}_2} \propto S_{\text{SO}_2} \quad (14)$$

The crucial difference to the SO₂ camera measurement is that instead of comparing the radiances of two separate spectral ranges averaged over a FWHM of ~ 10 nm, relative

Title Page

Abstract

Introduction

Conclusions

References

Tables

Figures

◀

▶

◀

▶

Back

Close

Full Screen / Esc

Printer-friendly Version

Interactive Discussion



FPI for SO₂ detection

J. Kuhn et al.

Title Page

Abstract

Introduction

Conclusions

References

Tables

Figures

◀

▶

◀

▶

Back

Close

Full Screen / Esc

Printer-friendly Version

Interactive Discussion



When using a FPI to measure SO₂ in the above described way, certain points have to be considered. In principle, changing δ leads to both a shift and a stretch of the spectral FPI transmission. However, once the order m of an observed transmission maximum at wavelength λ_m of the FPI is high enough, small changes in δ (Eq. 7) lead in a good approximation only to a wavelength shift of the transmission curve, while the stretch can be neglected ($\frac{\text{shift}}{\text{stretch}} = m + 1$). For a FPI transmission profile, which is matched to the SO₂ absorption cross section in the spectral range of interest (see Fig. 1), the order of the maxima is of about $m = \frac{2nd}{\lambda_m} \approx 140$. Therefore the change between FPI setting A (transmission maxima on SO₂ absorption bands) and B (transmission maxima between SO₂ absorption bands) can easily be realized by a small change of d , n or $\cos \alpha$.

In the following examination we assume that only the distance d of the FPI is varied for normal incident radiation ($\alpha = 0$) and $n = n_{\text{air}}$. Figure 3a shows the modeled optical density τ_{FPI} , measured by a FPI device as a function of d for a FPI surface reflectivity of 0.18, 0.65 and 0.74. An SO₂ slant column density of $S_{\text{SO}_2} = 10^{18}$ molec cm⁻² (400 ppm, at standard pressure and 20°C) was assumed, which is a common value measured at volcanic plumes. The oscillating behaviour of $\tau_{\text{FPI}}(d)$ mirrors the FPI transmission structure being shifted along the wavelength axis across the narrow band absorption structure of SO₂. FPI surface distances d corresponding to a maximum optical density (i.e. the FPI transmission maxima coincide with the SO₂ absorption bands) suggest values for d_A in setting A (e.g. 21.6 μm). The change $d_{AB} = d_B - d_A$ of the FPI surface distance required to reach setting B (minimum optical density, i.e. FPI transmission maxima in between SO₂ absorption bands) would be around 80 nm (for the adjoining minimum).

The modulation of τ_{FPI} as a function of d (Fig. 3a) increases with the reflectivity R (and thus with the finesse F) since the transmission maxima get sharper and therefore only radiation most affected by SO₂ absorption is transmitted. However, a higher finesse must be weighted against reduced integrated transmission of the FPI, i.e. reduced radiation throughput. Since less radiation arrives at the detector, the signal to

noise ratio $SNR = \frac{AA_{FPI}}{\Delta AA_{FPI}}$ starts to decrease again at values of R exceeding about 0.65, while AA_{FPI} increases monotonically (see Fig. 3b).

A similar compromise has to be made when choosing the cutoff wavelength λ_{cut} . The SO_2 absorption structure vanishes towards longer wavelengths, while the scattered solar radiance increases. Hence, there is also a certain value for λ_{cut} optimizing the SNR.

In order to be able to assess the noise ΔAA_{FPI} of a hypothetical instrument, we assumed $I_{FPI,i}$ and $I_{0,FPI,i}$ to be proportional to the number of photons reaching a hypothetical detector. Photon statistics then implies that the measurement error of the radiance is given by $\Delta I \propto \sqrt{I}$ and that the error in AA_{FPI} , ΔAA_{FPI} can be determined via Gaussian error propagation. The absolute value of the SNR is still dependent on the absolute radiances reaching the detector, which we don't know yet. Thus, in this theoretical study, SNR is used as a value proportional to the real SNR, which is sufficient for our optimization problems.

In order to find optimum parameters of a FPI set-up for normal incidence of radiation on the FPI ($\alpha = 0$), the SNR was optimized numerically. Table 1 shows the varied setup parameters and their values maximizing the SNR for an SO_2 column density of $S_{SO_2} = 10^{18} \text{ molec cm}^{-2}$.

Since δ is proportional to $\cos \alpha$ (Eq. 7), a small change of $\cos \alpha$ also causes a spectral shift of the FPI transmission structure T_{FPI} . Figure 4 shows the dependency of AA_{FPI} on α for the above proposed FPI setup and for $S_{SO_2} = 10^{18} \text{ molec cm}^{-2}$ (blue drawn line). The behaviour is mainly flat until reaching $\alpha_{max} \approx 1.8^\circ$, which constitutes a limitation for imaging instrument set-ups described below (see Sect. 4). For higher values of α the apparent absorbance AA_{FPI} oscillates between negative ($\tau_{FPI,A} < \tau_{FPI,B}$) and positive extrema attaining FPI incident angles α with vanishing AA_{FPI} in between them. Since the FPI transmission structures of the two settings (A and B) are shifted in the same way across several SO_2 absorption bands, both positive and negative values of AA_{FPI} carry the same SO_2 information. AA_{FPI} can thus be redefined as $|AA_{FPI}|$.

[Title Page](#)[Abstract](#)[Introduction](#)[Conclusions](#)[References](#)[Tables](#)[Figures](#)[◀](#)[▶](#)[◀](#)[▶](#)[Back](#)[Close](#)[Full Screen / Esc](#)[Printer-friendly Version](#)[Interactive Discussion](#)

3 Comparison to conventional SO₂ camera

The measurement principle as described up to now, could, e.g., be used to construct a simple “one pixle” (OP) FPI SO₂ detector with a rather narrow FOV. Such an instrument would indeed make sense since it would have a sensitivity and selectivity comparable to a spectrometer (as e.g. used in the Network of Observation of Volcanic and Atmospheric Change (NOVAC), see Galle et al., 2010), but could potentially be a more compact and more economic alternative. Likewise, the measurement principle of the filter based SO₂ camera could be adopted for an OP instrument. In the following we compare the performance of a OP FPI device with a hypothetical OP SO₂ “camera”. The conclusions drawn are also relevant for two-dimensional (2-D) cameras i.e. 2-D SO₂ cameras and 2-D FPI cameras as described in Sect. 4.

A FPI instrument with the parameters of Table 1 was considered, transmission curves of the corresponding settings are shown in Fig. 1. For the SO₂ camera the filter curves of Lübcke et al. (2013) were applied (see also Fig. 1). Moreover a second SO₂ camera set-up with filter A shifted by 5 nm towards shorter wavelengths is additionally examined for comparison to represent different popular set-ups of SO₂ cameras. In the following the shifted filter A is called filter A’.

3.1 Sensitivity to SO₂ and interference due to Mie scattering

Figure 5a shows the AA, for the respective measurement method as a function of the SO₂ column density S_{SO_2} . In order to examine the plume aerosol impact on the AA, two calibration curves were simulated for each device. The solid lines show the AA with SO₂ absorption being the only effect on $I_{S,0}(\lambda)$ (see Eq. 15). For the second set of lines (dashed) an additional wavelength dependent extinction $\tau_{\text{aerosol}}(\lambda)$ from a Mie scattering aerosol was assumed using an Ångström exponent of 1.2, which was found representative for volcanic plumes in the regarded spectral range (Spinetti and Buongiorno, 2007). The wavelength dependency of the aerosol extinction is then described by:

Title Page

Abstract

Introduction

Conclusions

References

Tables

Figures



Back

Close

Full Screen / Esc

Printer-friendly Version

Interactive Discussion



$$\tau_{\text{aerosol}}(\lambda) = \tau_{\text{aerosol},0}(\lambda_0) \cdot \lambda^{-1.2} \quad (17)$$

The aerosol optical density (AOD) was fixed to $\tau_{\text{aerosol},0} = 1$ at $\lambda_0 = 295$ nm, which corresponds to a rather moderate AOD of a volcanic plume.

The SO_2 camera with filter A' is more sensitive to SO_2 absorption since $\bar{\sigma}_{\text{SO}_2,A'} > \bar{\sigma}_{\text{SO}_2,A}$ (see Fig. 1 and Eq. 4). However, the increase of sensitivity comes together with a decrease of incoming solar radiance at shorter wavelengths.

$\tau_{\text{aerosol}}(\lambda)$ causes a higher extinction in the spectral ranges of filter A and A' than in the spectral range of filter B ($\tau_{\text{aerosol},A} > \tau_{\text{aerosol},B}$), leading to an offset $\Delta\text{AA}_{\text{AOD}}$ towards higher AA for the respective SO_2 camera set-ups. For $S_{\text{SO}_2} = 10^{18}$ molec cm^{-2} the assumed, small amount of aerosol thus accounts for relative deviations of $\frac{\Delta\text{AA}_{\text{AOD}}}{\text{AA}} \approx 54\%$ when using Filter A and $\frac{\Delta\text{AA}_{\text{AOD}}}{\text{AA}} \approx 38\%$ when using Filter A' . The smaller relative deviation for filter A' results from the different wavelength dependencies of aerosol extinction and SO_2 absorption.

The FPI device (drawn black line in Fig. 5a) is more sensitive to SO_2 than either of the two filter-based set-ups. This is because narrow band changes in the SO_2 absorption cross section below 310 nm are larger than the averaged cross sections $\bar{\sigma}_{\text{SO}_2,A'}$ and $\bar{\sigma}_{\text{SO}_2,A}$, respectively. For increasing S_{SO_2} the progression of AA_{FPI} slightly flattens since saturation effects at wavelengths of strong SO_2 absorption bands occur. However, there is hardly any sensitivity to the added amount of aerosol ($\frac{\Delta\text{AA}_{\text{FPI,AOD}}}{\text{AA}_{\text{FPI}}} < 1\%$ for $S_{\text{SO}_2} = 10^{18}$ molec cm^{-2}), in fact the dashed black line is almost completely covered by the black drawn line, meaning that $\tau_{\text{aerosol},\text{FPI},A} \approx \tau_{\text{aerosol},\text{FPI},B}$ still holds for the chosen FPI settings.

3.2 Ozone interference

Changes in the SZA between background and plume measurement induce changes in the lightpath of solar radiation through the stratospheric ozone layer. The absorption

Title Page

Abstract

Introduction

Conclusions

References

Tables

Figures



Back

Close

Full Screen / Esc

Printer-friendly Version

Interactive Discussion



cross section of ozone drastically increases towards shorter UV wavelengths in the observed spectral range. A changing background ozone column therefore will affect the above described SO₂ measurement principles.

The results of model calculations are shown in Fig. 5b, where again two curves are plotted for the three measurement set-ups. The solid lines again show the AA caused only by SO₂ absorption. The dashed lines represent the AA with an additional change of the ozone column density by $\Delta S_{O_3} = 100$ DU. This could for instance be caused by a change in the SZA from 30° to 48° in a 340DU atmosphere, occurring between the measurement and the last reference measurement.

The simulation again demonstrates that AA of the SO₂ cameras is much more strongly influenced by changes of the ozone background than AA_{FPI} of the FPI device. The relative deviations of AA for $S_{SO_2} = 10^{18}$ molec cm⁻² are $\frac{\Delta AA_{O_3}}{AA} \approx 110\%$ for both SO₂ camera implementations. The FPI device shows a significantly smaller deviation throughout the observed S_{SO_2} range. While for lower S_{SO_2} AA_{FPI} is slightly overestimated ($\frac{\Delta AA_{FPI, O_3}}{AA_{FPI}} \approx 3\%$ for $S_{SO_2} = 10^{18}$ molec cm⁻²), saturation at wavelength of strong SO₂ absorption bands and therefore flattening of the calibration curve occurs earlier.

4 FPI camera implementation

4.1 Scanning OP FPI camera

One possible way to obtain 2-D S_{SO_2} distributions is scanning a FOV with a OP FPI device, similar to scanning DOAS devices (e.g. whisk-broom IDOAS). A possible set-up for such a OP FPI instrument is proposed in Fig. 6a. The FPI is implemented by two plane parallel fused silica plates with reflective coatings at the inner surfaces. The separation d of the two plates is tunable by piezo actuators. The outer surfaces either carry anti-reflective coatings or are slightly tilted against each other to avoid additional interference effects. Lens 1, lens 2 and the aperture are chosen so that for a given

Title Page

Abstract

Introduction

Conclusions

References

Tables

Figures



Back

Close

Full Screen / Esc

Printer-friendly Version

Interactive Discussion



aperture angle ($2 \cdot \beta$) the restriction $\alpha < \alpha_{\max}$ holds for all beams arriving at the FPI. In such a set-up the maximum possible etendue E_{\max} is determined by α_{\max} and the illuminated FPI surface area.

In Table 2 the suggested OP FPI set-up is compared to a spectrometer commonly used in volcanic applications (Ocean Optics[®] USB 2000+) regarding the SNR (note that a telescope usually used with the spectrometer does not reduce the etendue, if well designed). In order to do this the relative radiances I_{FPI}^* and I_{spec}^* arriving at the detector of the respective instrument were estimated. Relative values of the maximum possible etendue E_{\max} (normalized to the spectrometer etendue), a loss factor η and the number N_I of radiance measurements needed to obtain one measurement of S_{SO_2} were taken into account. For the OP FPI device N_I can not exceed 0.5 since at least two radiance measurements (for setting A and B) are needed. Depending on how often a reference measurement (two additional radiance measurements) is recorded we find $N_I \in [0.25, 0.5]$. For the spectrometer a factor of $\eta = 0.5$ accounts for losses at the grating. A factor of $\eta = 0.2$ was assumed to account for FPI reflection and absorption. Other losses due to the employed optics were set to unity.

We assumed the FPI to be illuminated on a surface area of 20 mm diameter (e.g. $R_2 \approx 10$ mm) and $\alpha_{\max} = 1.8^\circ$, which for an aperture angle of $2 \cdot \beta = 1^\circ$ would require a radius $R_1 = 36$ mm of lens 1. For the USB 2000+ the limiting factors are the $f/4$ -optics of the spectrometer and the commonly chosen $1 \text{ mm} \times 50 \mu\text{m}$ entrance slit (assuming that the cylinder lens option in front of the detector is used, which focusses radiation from the complete height of the slit onto the detector). E_{\max} is then approximated by the product of the limiting surface area A_{lim} and the limiting solid angle Ω_{lim} .

For a measurement in the same spectral range the relative SNR would be proportional to $\sqrt{\frac{I_{\text{FPI}}^*}{I_{\text{spec}}^*}}$. According to our estimate the SNR of the OP FPI device is about 6–9 times higher. Thus, with the same SNR a 40–80 times higher temporal resolution (or associated spatial resolution) can be reached compared to a DOAS measurement. Of

FPI for SO₂ detection

J. Kuhn et al.

Title Page

Abstract

Introduction

Conclusions

References

Tables

Figures



Back

Close

Full Screen / Esc

Printer-friendly Version

Interactive Discussion



course the improved etendue of the FPI instrument can be used to obtain a combination of higher SNR (higher detection limit) and higher temporal resolution.

4.2 The 2-D FPI camera

While the use of a FPI in a OP detector has potentially large advantages over conventional spectrometers the FPI technique can also readily be used as a 2-D detector just like a SO₂ camera. In the following, two possible 2-D FPI SO₂ camera set-ups are briefly introduced.

4.2.1 FPI in a parallelized radiation set-up

Figure 6b shows a 2-D FPI camera set-up. Basically the implementation is similar to the OP FPI device. However, lens 1 is removed to increase the field of view to $FOV \approx 2 \cdot \beta = 2 \cdot \arctan \frac{R_2}{f_2}$ and the OP UV detector is replaced by a UV sensitive 2-D detector. The radiation from the FOV traverses the FPI parallelized ($\alpha < \alpha_{max}$) in order to avoid the dependence of AA_{FPI} on β . Evidently, the etendue per pixel is thereby drastically reduced compared to the OP FPI instrument.

This set-up (with band-pass interference filters instead of the FPI) was already employed for a SO₂ camera by Kern et al. (2010b), with a comparable entrance aperture (i.e. maximum incidence angle on the filters $\approx \alpha_{max}$) and, thus, comparable etendue. However, for a FPI SO₂ camera the radiance reaching the detector is by a factor of ~ 30 – 50 smaller (due to FPI reflection and the measurement at shorter wavelengths, see Fig. 1). Even for the by a factor of ~ 2 higher sensitivity (see Fig. 5) of the FPI camera the SNR would be distinctly lower. Nevertheless, reduced interference with plume AOD and ozone background variation (see Sect. 3) may outweigh a reduced SNR (higher accuracy at lower precision).

Title Page

Abstract

Introduction

Conclusions

References

Tables

Figures

◀

▶

◀

▶

Back

Close

Full Screen / Esc

Printer-friendly Version

Interactive Discussion



4.2.2 High etendue vs. sensitivity structure

Another implementation of a 2-D FPI camera achieving much higher light throughput is depicted in Fig. 6c. The FPI and the band-pass filter are mounted in front of a lens (lens 3), similar to the SO₂ camera set-up of e.g. Mori and Burton (2006). For a FOV_≈ 20° the etendue is thereby increased by a factor of about 32 compared to the set-up described in Sect. 4.2.1, because the radiation is not parallelized anymore. The maximum incident angle α on the FPI is now determined by the angle $\beta = \frac{\text{FOV}}{2}$. Each detector pixel is observing a small, comparable set of incident angles α . However, for a measurement involving two FPI surface distances the large range of incident angles $\alpha \in [0^\circ, 10^\circ]$ leads to rings of equal, partly vanishing SO₂ sensitivity on the 2-D detector (see Figs. 4 and 7b). To obtain a more or less constant SO₂ sensitivity for the entire FOV (for the entire detector surface) a measurement has to employ more than two FPI settings (e.g. more than two FPI surface distances d). Figure 7 shows how employing a set of measurements with four different values of the FPI surface distance d arranged in two pairs (d_A and $d_B = d_A + d_{AB}$, $d_C = d_A + \frac{1}{2}d_{AB}$ and $d_D = d_A + \frac{3}{2}d_{AB}$) leads to a SO₂ sensitivity varying by only about 32% across the entire FOV. By increasing the number of measurements with different FPI settings the sensitivity distribution on the 2-D detector can be further smoothed.

5 Conclusions

We proposed a remote sensing method to measure volcanic gas emissions using their regular absorption features in the UV wavelength region. The advantage of a Fabry–Perot interferometer used in this method is that its spectral transmittance can be tuned to precisely match the absorption bands of the trace gas of interest. In our theoretical considerations parameters of the FPI were specified for SO₂ and possible implementations of measurement set-ups were discussed.

Title Page

Abstract

Introduction

Conclusions

References

Tables

Figures



Back

Close

Full Screen / Esc

Printer-friendly Version

Interactive Discussion



FPI for SO₂ detection

J. Kuhn et al.

[Title Page](#)[Abstract](#)[Introduction](#)[Conclusions](#)[References](#)[Tables](#)[Figures](#)[Back](#)[Close](#)[Full Screen / Esc](#)[Printer-friendly Version](#)[Interactive Discussion](#)

We presented model calculations and compared the FPI method with the interference filter-based SO₂ camera method. The FPI method exhibits a 1.3–2.5 times higher SO₂ sensitivity. Moreover, a far higher measurement accuracy due to reduced dependence on radiative transfer is reached. For instance at $S_{\text{SO}_2} = 10^{18}$ molec cm⁻² the deviations of the AA of SO₂ cameras were 38–54 % for a low plume AOD of approximately 1 and 110 % for an ozone background change of $\Delta S_{\text{O}_3} = 100$ DU. In comparison AA_{FPI} deviated by only < 1 % and 3 %, respectively.

As a one-pixel application the introduced FPI technique has a higher radiation throughput compared to a common miniature spectrometer, while being of comparable size and weight. Thus a better SNR is obtained and/or much faster measurements are feasible, while the selectivity and immunity to plume AOD and ozone background interferences are still quite good.

Three different imaging implementations were introduced. The first approach uses an optical system that ensures perpendicular illumination of the FPI. In a second approach a higher radiation throughput is reached by allowing a larger aperture, leading to a non-perpendicular FPI illumination. The resulting variations of the sensitivity across the detector can be partly overcome by using more than two FPI settings. A third implementation is based on the whisk-broom imaging approach using an OP FPI device.

Besides SO₂ the technique discussed in this paper can potentially be applied to study other gases with regular spaced narrow-band absorption in the UV/VIS – like e.g. BrO, OClO, or IO.

Acknowledgement. We acknowledge financial support by Deutsche Forschungsgemeinschaft and Ruprecht-Karls-Universität Heidelberg within the funding programme Open Access Publishing.

References

Barrett, J. J. and Myers, S. A.: New interferometric method for studying periodic spectra using a Fabry–Perot interferometer, *J. Opt. Soc. Am.*, 61, 1246–1251, 1971. 5120

FPI for SO₂ detection

J. Kuhn et al.

Title Page

Abstract

Introduction

Conclusions

References

Tables

Figures



Back

Close

Full Screen / Esc

Printer-friendly Version

Interactive Discussion



- Bluth, G., Shannon, J., Watson, I., Prata, A., and Realmuto, V.: Development of an ultra-violet digital camera for volcanic SO₂ imaging, *J. Volcanol. Geotherm. Res.*, 161, 47–56, 2007. 5119
- Bobrowski, N., Hönninger, G., Lohberger, F., and Platt, U.: IDOAS: a new monitoring technique to study the 2-D distribution of volcanic gas emissions, *J. Volcanol. Geoth. Res.*, 150, 329–338, 2006. 5119
- Bogumil, K., Orphal, J., Homann, T., Voigt, S., Spietz, P., Fleischmann, O., Vogel, A., Hartmann, M., Bovensmann, H., Frerick, J., and Burrows, J.: Measurements of molecular absorption spectra with the SCIAMACHY pre-flight model: instrument characterization and reference data for atmospheric remote sensing in the 230–2380 nm region, *J. Photochem. Photobiol. A*, 157, 167–184, 2003. 5125, 5139
- Galle, B., Johansson, M., Rivera, C., Zhang, Y., Kihlman, M., Kern, C., Lehmann, T., Platt, U., Arellano, S., and Hidalgo, S.: Network for Observation of Volcanic and Atmospheric Change (NOVAC) – A global network for volcanic gas monitoring: network layout and instrument description, *J. Geophys. Res. D*, 115, D05304, doi:10.1029/2009JD011823, 2010. 5118, 5119, 5128
- Hönninger, G., von Friedeburg, C., and Platt, U.: Multi axis differential optical absorption spectroscopy (MAX-DOAS), *Atmos. Chem. Phys.*, 4, 231–254, doi:10.5194/acp-4-231-2004, 2004. 5119
- Kern, C., Deutschmann, T., Vogel, L., Wöhrbach, M., Wagner, T., and Platt, U.: Radiative transfer corrections for accurate spectroscopic measurements of volcanic gas emissions, *B. Volcanol.*, 72, 233–247, 2010a. 5119
- Kern, C., Kick, F., Lübcke, P., Vogel, L., Wöhrbach, M., and Platt, U.: Theoretical description of functionality, applications, and limitations of SO₂ cameras for the remote sensing of volcanic plumes, *Atmos. Meas. Tech.*, 3, 733–749, doi:10.5194/amt-3-733-2010, 2010b. 5119, 5120, 5132
- Kern, C., Werner, C., Elias, T., Sutton, A. J., and Lübcke, P.: Applying UV cameras for SO₂ detection to distant or optically thick volcanic plumes, *J. Volcanol. Geotherm. Res.*, 262, 80–89, 2013. 5119
- Kuhn, J.: Fernerkundung von Schwefeldioxid mit einem Fabry–Perot Interferometer, B.S. thesis, University of Heidelberg, 2012. 5119
- Louban, I., Bobrowski, N., Rouwet, D., Inguaggiato, S., and Platt, U.: Imaging DOAS for volcanological applications, *B. Volcanol.*, 71, 753–765, 2009. 5119

FPI for SO₂ detection

J. Kuhn et al.

[Title Page](#)[Abstract](#)[Introduction](#)[Conclusions](#)[References](#)[Tables](#)[Figures](#)[Back](#)[Close](#)[Full Screen / Esc](#)[Printer-friendly Version](#)[Interactive Discussion](#)

- Lübcke, P., Bobrowski, N., Illing, S., Kern, C., Alvarez Nieves, J. M., Vogel, L., Zielcke, J., Delgado Granados, H., and Platt, U.: On the absolute calibration of SO₂ cameras, *Atmos. Meas. Tech.*, 6, 677–696, doi:10.5194/amt-6-677-2013, 2013. 5119, 5120, 5122, 5128
- Moffat, A. J. and Millan, M. M.: The applications of optical correlation techniques to the remote sensing of SO₂ plumes using sky light, *Atmos. Environ.*, 5, 677–690, 1971. 5118
- Mori, T. and Burton, M.: The SO₂ camera: A simple, fast and cheap method for ground-based imaging of SO₂ in volcanic plumes, *Geophys. Res. Lett.*, 33, L24804, doi:10.1029/2006GL027916, 2006. 5119, 5122, 5133
- Nadeau, P. A., Palma, J. L., and Waite, G. P.: Linking volcanic tremor, degassing, and eruption dynamics via SO₂ imaging, *Geophys. Res. Lett.*, 38, L01304, doi:10.1029/2010GL045820, 2011. 5119
- Oppenheimer, C., Francis, P., and Stix, J.: Depletion rates of sulfur dioxide in tropospheric volcanic plumes, *Geophys. Res. Lett.*, 25, 2671–2674, 1998. 5118
- Perot, A. and Fabry, C.: On the application of interference phenomena to the solution of various problems of spectroscopy and metrology, *Astrophys. J.*, 9, 87–115, 1899. 5123
- Platt, U. and Stutz, J.: *Differential Optical Absorption Spectroscopy: Principles and Applications (Physics of Earth and Space Environments)*, Springer, 2008. 5118
- Spinetti, C. and Buongiorno, M.: Volcanic aerosol optical characteristics of Mt. Etna tropospheric plume retrieved by means of airborne multispectral images, *J. Atmos. Sol.-Terr. Phys.*, 69, 981–994, 2007. 5128
- Textor, C., Graf, H., Timmreck, C. and Robock, A.: Emissions from volcanoes, in: *Emissions of Atmospheric Trace Gas Compounds*, Kluwer, Dordrecht, 296–303, 2004. 5118
- Vargas-Rodriguez, E. and Rutt, H. N.: Design of CO, CO₂ and CH₄ gas sensors based on correlation spectroscopy using a Fabry–Perot interferometer, *Sensor Actuat. B-Chem.*, 137, 410–419, 2009. 5120
- von Glasow, R., Bobrowski, N., and Kern, C.: The effects of volcanic eruptions on atmospheric chemistry, *Chem. Geol.*, 263, 131–142, 2009. 5118
- Wilson, E. L., Georgieva, E. M., and Heaps, W. S.: Development of a Fabry–Perot interferometer for ultra-precise measurements of column CO₂, *Meas. Sci. Technol.*, 18, 1495–1502, 2007. 5120

FPI for SO₂ detection

J. Kuhn et al.

Title Page

Abstract

Introduction

Conclusions

References

Tables

Figures

◀

▶

◀

▶

Back

Close

Full Screen / Esc

Printer-friendly Version

Interactive Discussion



Table 1. Result of the numerical optimization of the SNR of a FPI SO₂ measurement for $S_{\text{SO}_2} = 10^{18} \text{ molec cm}^{-2}$; d_A is the distance of the surfaces in FPI setting A, d_{AB} the change in surface distance to get from FPI setting A to FPI setting B, F the finesse and λ_{cut} the cutoff wavelength of the band pass filter towards longer wavelengths.

parameter	maximizing value
d_A	21.6 μm
d_{AB}	84 nm
R	0.65 ($F = 7.1$)
λ_{cut}	310 nm

FPI for SO₂ detection

J. Kuhn et al.

Table 2. Comparison of the OP FPI camera and a spectrometer used in DOAS measurements (Ocean Optics® USB 2000+), when observing the same spectral range: The surface area A_{lim} and the solid angle Ω_{lim} limiting the etendue E_{max} are mainly contributing to the 6–9 times higher SNR of the OP FPI camera.

	OP FPI device	spectrometer (DOAS)
A_{lim}	314 mm ²	0.05 mm ²
Ω_{lim}	3.1×10^{-3} sr	49×10^{-3} sr
$A_{\text{lim}} \times \Omega_{\text{lim}}$	973×10^{-3} mm ² sr	2.4×10^{-3} mm ² sr
E_{max}	400	1
rel. η	0.2	0.5
N_l	0.25–0.5	1
$\frac{I_{\text{FPI}}^*}{I_{\text{spec}}^*}$		40–80
$\sqrt{\frac{I_{\text{FPI}}^*}{I_{\text{spec}}^*}} \approx \frac{\text{SNR}_{\text{FPI}}}{\text{SNR}_{\text{spec}}}$		6–9

Title Page

Abstract

Introduction

Conclusions

References

Tables

Figures

◀

▶

◀

▶

Back

Close

Full Screen / Esc

Printer-friendly Version

Interactive Discussion



FPI for SO₂ detection

J. Kuhn et al.

Title Page

Abstract

Introduction

Conclusions

References

Tables

Figures



Back

Close

Full Screen / Esc

Printer-friendly Version

Interactive Discussion

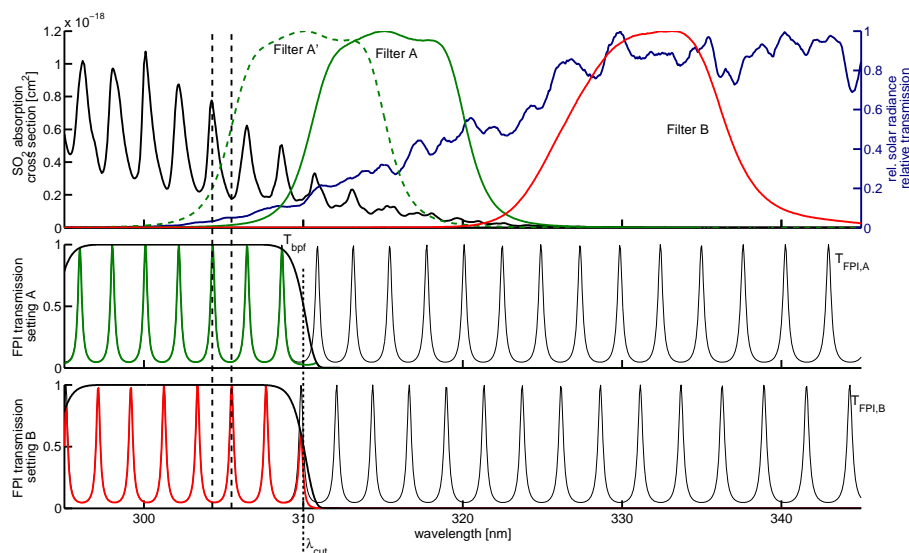


Figure 1. Upper panel: SO₂ absorption cross section (black drawn line, left ordinate axis, data from Bogumil et al., 2003), incident solar radiance (blue drawn line, right ordinate axis) as a function of wavelength, and transmission curves of Filter A, A' and B (right ordinate axis); Lower panels: FPI transmission curve for settings A and B; the dashed vertical lines mark positions at which FPI transmission maxima coincide with maximum and minimum absorption, respectively.

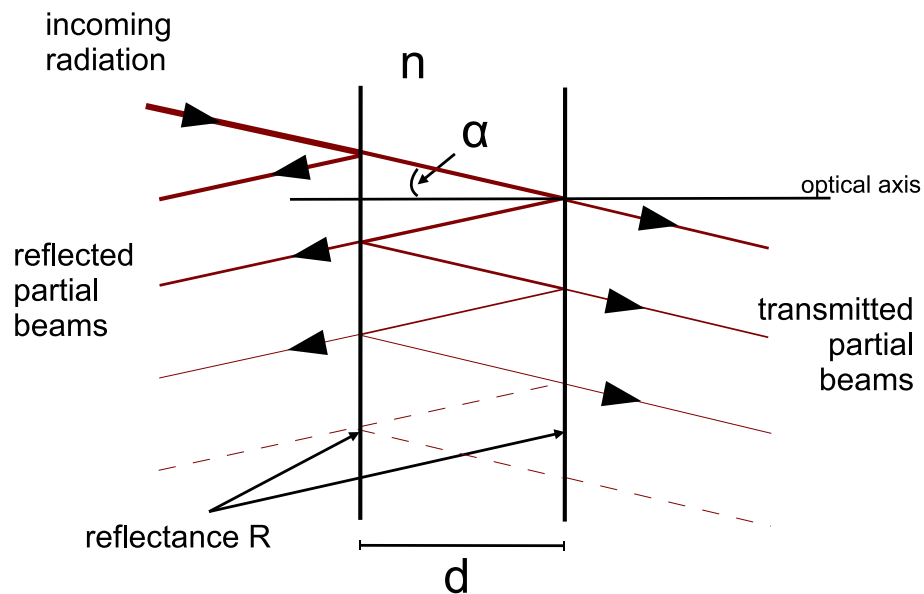
[Title Page](#)
[Abstract](#)
[Introduction](#)
[Conclusions](#)
[References](#)
[Tables](#)
[Figures](#)
[◀](#)
[▶](#)
[◀](#)
[▶](#)
[Back](#)
[Close](#)
[Full Screen / Esc](#)
[Printer-friendly Version](#)
[Interactive Discussion](#)


Figure 2. Fabry Perot interferometer: incoming radiation undergoes multiple reflections between two plane parallel surfaces of reflectance R , mounted at distance d . Interference of the transmitted partial beams leads to the transmission structure (see Eq. 8, Fig. 1), which can be optimized to match periodic absorption structures.

FPI for SO₂ detection

J. Kuhn et al.

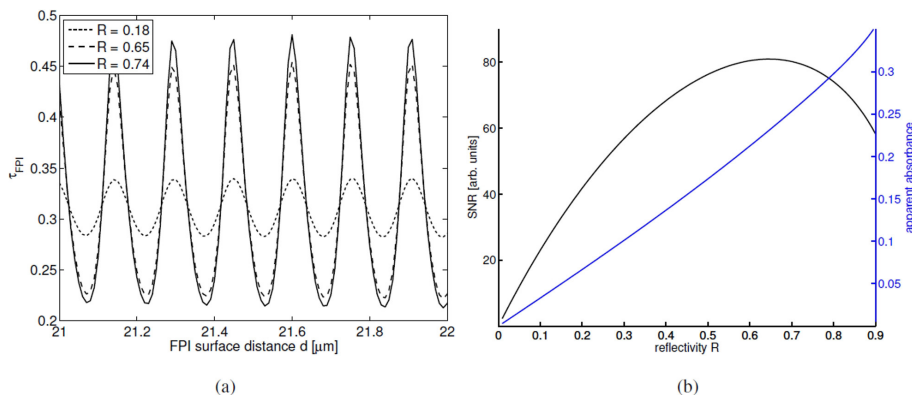


Figure 3. (a) Optical density τ for an SO₂ slant column density $S_{\text{SO}_2} = 10^{18} \text{ molec cm}^{-2}$ observed by a FPI setup for varying surface distance d , calculated for a FPI reflectivity of 0.18, 0.65 and 0.74. The difference of the optical densities recorded at maximum (d_A at e.g. 21.6 μm) and minimum (d_B) values is the apparent absorbance. (b) The apparent absorbance (blue line) grows monotonically with the reflectivity R . However, for high R (and thus for high F) the SNR is decreasing, since less radiation is transmitted.



Back

Close

Full Screen / Esc

Printer-friendly Version

Interactive Discussion



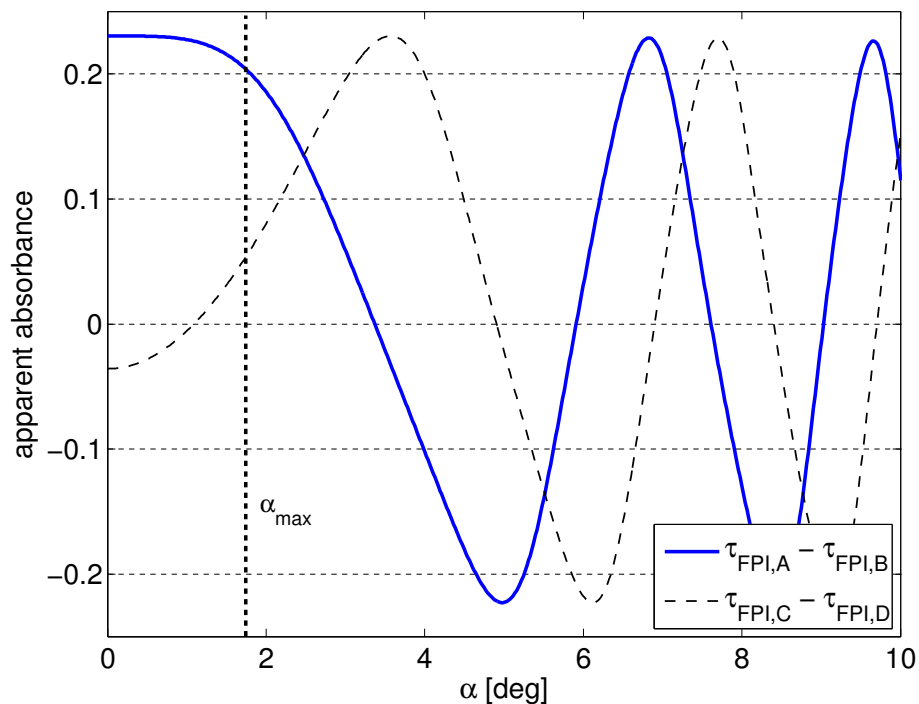


Figure 4. AA_{FPI} as a function of the incident illumination angle α for an SO_2 slant column density of $S_{\text{SO}_2} = 10^{18} \text{ molec cm}^{-2}$ (blue drawn line): Small changes in $\cos \alpha$ cause a shift of T_{FPI} in wavelength, which leads to an oscillating progression of AA_{FPI} over α . $\alpha_{\text{max}} \approx 1.8^\circ$ limits the range of angles for the assumption of parallel incident radiation. The dashed line shows, a measurement with two different FPI surface distances ($d_{\text{C}} = d_{\text{A}} + \frac{1}{2}d_{\text{AB}}$ and $d_{\text{D}} = d_{\text{A}} + \frac{3}{2}d_{\text{AB}}$). By using more than two FPI settings sensitivity for arbitrary incidence angles can be obtained (see Sect. 4).

Title Page

Abstract

Introduction

Conclusions

References

Tables

Figures

◀

▶

◀

▶

Back

Close

Full Screen / Esc

Printer-friendly Version

Interactive Discussion



FPI for SO₂ detection

J. Kuhn et al.

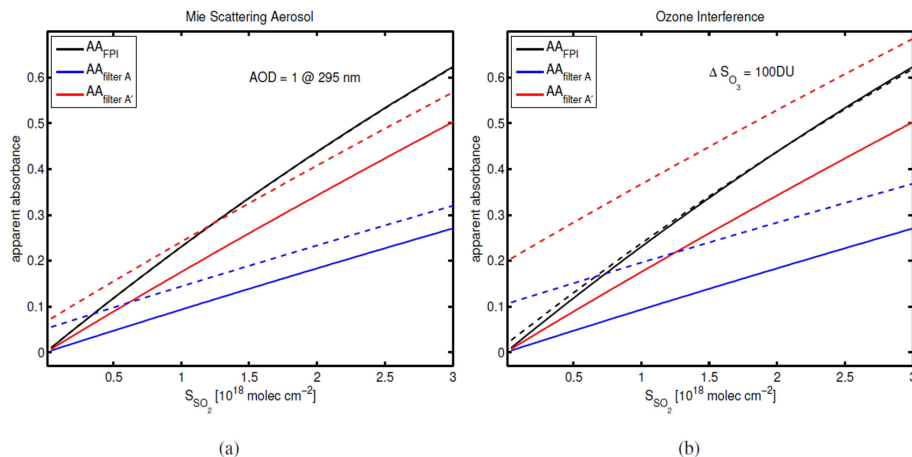


Figure 5. Modelled calibration curves (without aerosol) for the OP FPI SO₂ device (black drawn line) and the OP filter-based SO₂ devices with filter A (blue drawn line) and filter A' (red drawn line); **(a)** deviation (dashed lines) due to Mie scattering aerosol with an optical density (AOD) of 1 at 295 nm. The filter-based SO₂ devices (regardless of the filter used) show a considerable false positive SO₂ signal, while the curve for the FPI device hardly separates from the undisturbed calibration curve. **(b)** Deviation due to ozone interference, where a change of ΔS_{O₃} = 100DU was assumed. Again the FPI measurement shows far less deviation.

Title Page

Abstract

Introduction

Conclusions

References

Tables

Figures

◀

▶

◀

▶

Back

Close

Full Screen / Esc

Printer-friendly Version

Interactive Discussion



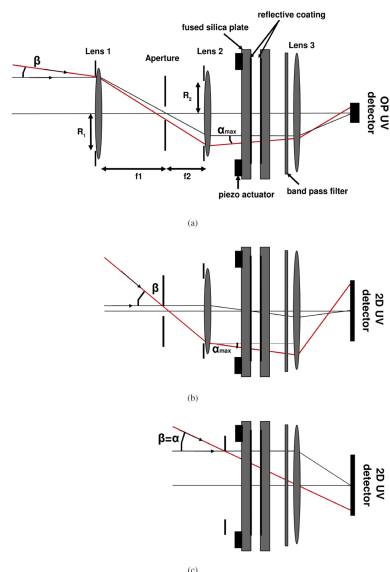


Figure 6. Three possible implementations of a FPI camera. In each set-up the FPI is implemented by two fused silica plates with reflective coatings (reflectivity R) at the inner surfaces, whose separation d is tunable by piezo actuators. The outer surfaces either carry anti-reflective coating or are slightly tilted against each other to exclude additional interference effects. **(a)** One Pixel FPI instrument: Two lenses (lens 1, lens 2) and an aperture determine the aperture angle ($2 \cdot \beta$) of the instrument, constraint by α_{\max} . Lens 3 projects the radiation onto a UV sensitive OP detector after having passed the band-pass filter. 2-D data is achieved by scanning, either by additional optics or by tilting the whole device. **(b)** 2-D FPI camera, where radiation from FOV is parallelized before being projected onto a 2-D detector. **(c)** 2-D FPI camera, where radiation from FOV traverses the FPI under $\alpha = \beta$ for $\text{FOV} \approx 20^\circ$. More than two FPI settings are required to obtain non-vanishing sensitivity throughout the FOV (see Fig. 7).

[Title Page](#)
[Abstract](#)
[Introduction](#)
[Conclusions](#)
[References](#)
[Tables](#)
[Figures](#)
[◀](#)
[▶](#)
[◀](#)
[▶](#)
[Back](#)
[Close](#)
[Full Screen / Esc](#)
[Printer-friendly Version](#)
[Interactive Discussion](#)

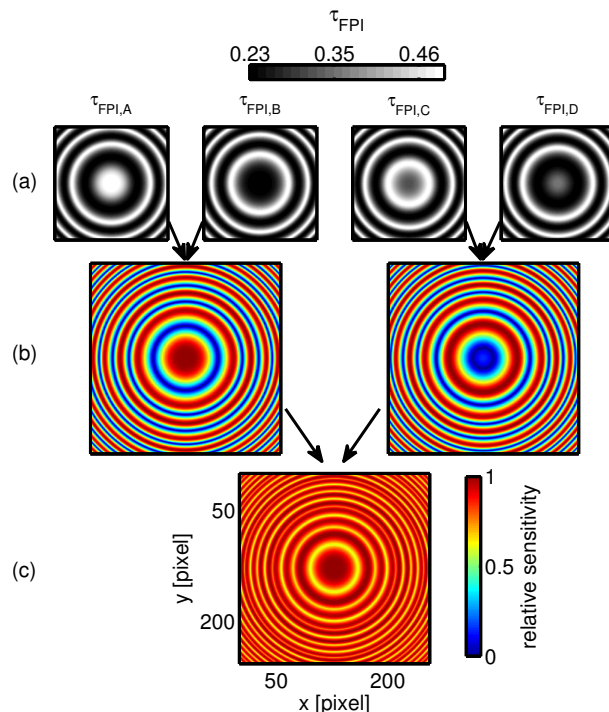



Figure 7. To obtain non-vanishing sensitivity throughout the entire FOV the FPI camera set-up shown in Fig. 6c requires more than two measurement settings. **(a)** distribution of τ_{FPI} on a 2-D detector for FOV $\approx 20^\circ$ and two different FPI surface distance pairs (d_A and $d_B = d_A + d_{\text{AB}}$, $d_C = d_A + \frac{1}{2}d_{\text{AB}}$ and $d_D = d_A + \frac{3}{2}d_{\text{AB}}$). A homogeneous S_{SO_2} distribution of 10^{18} molec cm^{-2} was assumed. **(b)** Relative sensitivity distributions calculated for each of the d -pairs with rings of vanishing sensitivity (blue) at different radii from the detector center. **(c)** Combining the distributions of **(b)** yields non-vanishing sensitivity throughout the entire FOV. By increasing the number of measurements with different FPI settings the sensitivity distribution on the detector can be further smoothed.